

capture the true distribution of biological information [30].

Recently, there has been an attempt to integrate user feedback through RLHF in order to increase the medical plausibility of generated images [30]. However, that still leaves us with a two-stage process with the second stage involving experts' feedback which is costly and time-consuming.

In this work, we demonstrate that the medical plausibility of generated images can be increased substantially without the need for experts' feedback. This could dramatically reduce the cost and time required for medical image generation.

Summary of our key contributions:

- 1) We propose a new prototype guided diffusion model-based medical image generation pipeline that increases the biological accuracy of medical images generated.
- 2) We generate images for bone-marrow and dermatology datasets and demonstrate that increase in biological plausibility is consistent across two different domains.

2. Related Works

2.1. Prototype Learning

Recently, prototype learning utilizing deep networks has caught the attention of researchers and has been applied for a range of tasks through enhancing of the feature space by learning clusters (prototypes) of different classes/categories. Zhou et al [36] improved upon semantic segmentation through the representation of different semantic classes with prototypes. Snell et al [27] proposed prototype learning for a few-shot classification problem whereas Shu et al [26] devised a prototypical network for an open set recognition task. Prototypes have been integrated into both supervised [34] as well as unsupervised [11] classification tasks. Kim et al [16] learn a discrete space that included prototypes for image reconstruction tasks. Improvements have been made in prototype learning architecture as well. Du et al [9] introduce ProtoDiff, a novel framework that leverages a task-guided diffusion model during the meta-training phase to gradually generate prototypes, thereby providing efficient class representations.

2.2. Diffusion Models

Diffusion models are generative models that have recently shown great promise in their capability to generate high-fidelity images for a variety of applications. Decreased sampling times [24, 29] and architectural improvements such as cascaded diffusion [14] have been proposed to improve the generative ability of diffusion models. In parallel, a new area of research has focused on conditioning the diffusion models through text and images. This conditioning helps in maintaining control over the diffusion process and results in the improvement of generation quality.

Traditionally, the conditioning information is embedded in the latent space through an encoder such as CLIP [21] or VQGAN [10]. Retrieval Augmented Diffusion [4] conditions the generation process on the neighbors of an image. Our method has a similar intuition as learned prototypes have a similar advantage in capturing latent information of a class as neighboring images may have.

2.3. Diffusion Models for medical image generation

The traditional approach for medical image generation has been to finetune a diffusion model using sufficient samples from a given modality. Diffusion probabilistic models [8] have recently shown great promise in the generation of high-fidelity medical images [18]. Ali et al [2] showed that Stable Diffusion can generate high-quality X-Ray and CT images. Latent diffusion models [20] have been used for generating synthetic images from 3D brain images.

Traditionally, these generative models for medical images are evaluated either indirectly through downstream classification tasks or directly through metrics such as FID scores [12]. Other approaches involve sample-level evaluation metrics such as precision and recall [23] which check if synthetic samples reside in support of real data distribution. However, these approaches fail to incorporate biological/medical information [30] which is of paramount importance while evaluating the medical plausibility of generated images. There are some traditional metrics for medical image evaluation such as signal-to-noise ratio and contrast-to-noise ratio [32] which are applied to real images and cannot be repurposed for evaluation of synthetic medical images. Evaluating synthetic images could be quite challenging as we do not have any ground truth as to what is medically plausible and what is not. Therefore it becomes imperative to design robust evaluation criteria that are domain-specific and capture different dimensions specific to the domain. In the medical domain, this entails getting expert feedback to ascertain the biological/medical plausibility of generated images. Sun et al [30] were the first to introduce human feedback as the gold standard for the evaluation of synthetically generated images. Further, they showed that the biological plausibility of the generated images increases dramatically once human feedbacks are integrated through RLHF.

3. Background

3.1. Diffusion Models

Gaussian diffusion models have become a prominent generative method since their introduction by [28]. These models have inspired numerous variants based on the diffusion concept. During the training phase, Gaussian noise is incrementally added to a sample from the real data distribu-

tion $x_0 \sim q(x)$ over T time steps:

$$q(x_t | x_{t-1}) = \mathcal{N}(x_t; \sqrt{1 - \beta_t}x_{t-1}, \beta_t I) \quad (1)$$

Here, x_{t-1} is transformed into x_t by adding Gaussian noise at the t -th time step. The variance of the added noise is β_t and $\sqrt{1 - \beta_t}$ is the scaling parameter based on a variance schedule. To obtain x_t at any arbitrary time step t without iterating t steps, a reparameterization trick, leveraging properties of the Gaussian distribution, can be applied:

$$q(x_t | x_0) = \mathcal{N}(x_t; \sqrt{\bar{\alpha}_t}x_0, (1 - \bar{\alpha}_t)I) \quad (2)$$

$$x_t = \sqrt{\bar{\alpha}_t}x_0 + \sqrt{1 - \bar{\alpha}_t}\epsilon \quad (3)$$

In these equations, $\alpha_t = 1 - \beta_t$, $\bar{\alpha}_t = \prod_{i=1}^t \alpha_i$, and $\epsilon \sim \mathcal{N}(0, I)$. The training phase of diffusion models involves a denoising process to reverse the noising process in Equation 1. This denoising process is defined as:

$$p_\theta(x_{t-1} | x_t) = \mathcal{N}(x_{t-1}; \mu_\theta(x_t, t), \Sigma_\theta(x_t, t)) \quad (4)$$

Here, θ represents the parameters of a neural network that predicts the mean $\mu_\theta(x_t, t)$ and variance $\Sigma_\theta(x_t, t)$ of the Gaussian distribution. Starting from pure Gaussian noise x_T , the image x_0 is obtained by progressively reducing the noise over T time steps. The main goal of diffusion models as generative models is to learn this reverse process to generate a high-quality image x_0 from random noise x_T .

In Denoising Diffusion Probabilistic Models (DDPM) [13], the mean $\mu_\theta(x_t, t)$ is learned while the variance $\Sigma_\theta(x_t, t)$ is kept constant. A tractable variational lower bound exists for optimizing the neural network in Equation 4. [13] decompose the objective function and demonstrate that predicting the noise ϵ added in the current time step, as in Equation 2, is the optimal way to parameterize the model's mean $\mu_\theta(x_t, t)$:

$$\mu_\theta(x_t, t) = \frac{1}{\sqrt{\alpha_t}} \left(x_t - \frac{\beta_t}{\sqrt{1 - \bar{\alpha}_t}} \epsilon_\theta(x_t, t) \right) \quad (5)$$

The simplified training objective is derived as:

$$L_{\text{simple}} = \mathbb{E}_{t \sim [1, T], x_0 \sim q(x), \epsilon \sim \mathcal{N}(0, I)} [\|\epsilon - \epsilon_\theta(x_t, t)\|^2] \quad (6)$$

While DDPM generates unconditional images, guided diffusion models are also used for conditional image generation. [8] propose classifier guidance, where the class-conditional parameters $\mu_\theta(x_t | y)$ and $\Sigma_\theta(x_t | y)$ are adjusted using the gradients of a classifier $p_\phi(y | x_t)$ predicting the target class y . The perturbed mean with the guidance scale s is:

$$\mu_\theta(x_t | y) = \mu_\theta(x_t | y) + s \Sigma_\theta(x_t | y) \nabla_{x_t} \log p_\phi(y | x_t) \quad (7)$$

Despite improving image quality, classifier guidance has its challenges. As the denoising process starts with highly noisy input and proceeds with noisy images for most time steps, the classifier must be robust to noise. Obtaining such a classifier is difficult, and predicting a class label does not require most of the data's information, potentially misleading the generation direction.

[15] propose a classifier-free guidance method, eliminating the need for a separate classifier. The conditioning information y is periodically used, and dropped out at other times, allowing a single model for both unconditional and conditional generation. They derive that unconditional $\epsilon_\theta(x_t, t)$ and conditional $\epsilon_\theta(x_t, t, y)$ estimations represent the classifier's gradients as:

$$\begin{aligned} \nabla_{x_t} \log p(y | x_t) &= \nabla_{x_t} \log p(x_t | y) - \nabla_{x_t} \log p(x_t) \\ &= -\frac{1}{\sqrt{1 - \bar{\alpha}_t}} (\epsilon_\theta(x_t, t, y) - \epsilon_\theta(x_t, t)) \end{aligned} \quad (8)$$

Equation 8 suggests that an implicit classifier can replace the need for an explicit one, with [15] reporting better results with classifier-free guidance.

Our work utilizes the method proposed by [3] to improve the generation performance by utilizing prototype learning.

3.2. Prototype Learning

Prototype learning is a foundational concept in machine learning that enhances the interpretability and robustness of classification models by utilizing representative examples, or prototypes, for each class. These prototypes serve as central reference points that capture the essential characteristics of their respective classes. Unlike traditional methods that rely solely on raw data or hand-engineered features, prototype learning integrates these learned prototypes into the classification process, thereby improving both accuracy and resilience to unseen data.

The study draws upon the pioneering work of [35], which introduced convolutional prototype learning (CPL) within deep convolutional neural networks (CNNs). Yang et al. proposed a framework where CNNs act as feature extractors $f(x; \theta)$, extracting high-level features from raw medical images x . Rather than employing a softmax layer for classification, CPL maintains and learns several prototypes m_{ij} for each class i , enhancing the model's ability to generalize beyond the training data.

In the CPL framework, the distance is used to measure the similarity between the samples and the prototypes. Consequently, the probability of a sample (x, y) belonging to

the prototype m_{ij} is determined by the distance between them:

$$p(x \in m_{ij}|x) \propto -\|f(x) - m_{ij}\|_2^2. \quad (9)$$

To ensure the probability is non-negative and sums to one, the probability $p(x \in m_{ij}|x)$ is defined as:

$$p(x \in m_{ij}|x) = \frac{e^{-\gamma d(f(x), m_{ij})}}{\sum_{k=1}^C \sum_{l=1}^K e^{-\gamma d(f(x), m_{kl})}}, \quad (10)$$

where $d(f(x), m_{ij}) = \|f(x) - m_{ij}\|_2^2$ represents the distance between $f(x)$ and m_{ij} . γ is a hyper-parameter that controls the hardness of probability assignment. Given this definition, the probability $p(y|x)$ is expressed as:

$$p(y|x) = \sum_{j=1}^K p(x \in m_{yj}|x). \quad (11)$$

Based on the probability $p(y|x)$, the cross entropy (CE) loss in the CPL framework is defined as:

$$l((x, y); \theta, M) = -\log p(y|x). \quad (12)$$

This loss function is based on distance, differentiating it from traditional cross-entropy loss, and is thus referred to as distance-based cross-entropy (DCE) loss. From Equations (12), (13), and (14), minimizing the loss function essentially reduces the distance between the samples and the prototypes of their true classes. The DCE is also derivable with respect to M and f .

Additionally, a prototype loss (PL) is introduced to refine the optimization process by decreasing distances between features and their corresponding prototypes, thereby promoting both intra-class compactness and inter-class separability. The prototype loss is defined as:

$$pl((x, y); \theta, M) = \|f(x) - m_{yj}\|_2^2, \quad (13)$$

where m_{yj} is the closest prototype to $f(x)$ from the corresponding class y . The prototype loss is combined with the classification loss to train the model, resulting in the total loss:

$$\text{loss}((x, y); \theta, M) = l((x, y); \theta, M) + \lambda pl((x, y); \theta, M), \quad (14)$$

where λ is a hyper-parameter controlling the weight of the prototype loss.

By integrating these losses, the CPL framework achieves intra-class compactness and inter-class separability, which are crucial for robust classification and generalization to new classes.

4. Proposed Method

Our proposed method leverages prototype-guided diffusion models for zero-shot conditional image generation. We

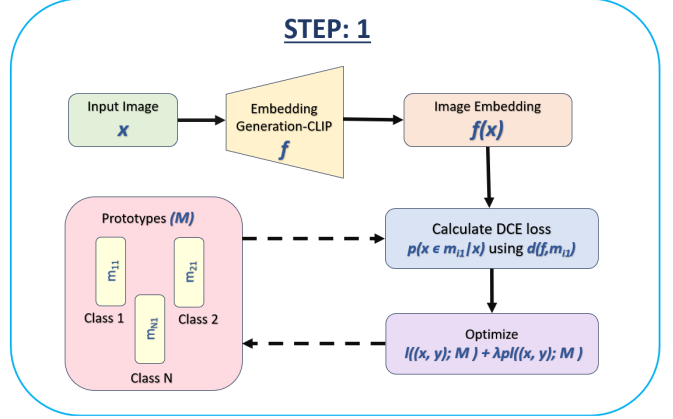


Figure 1. Prototype generation represents the first step of the training process, here a Codebook(M) of prototypes is learned

use predefined prototypes to guide the diffusion process, ensuring that the generated images adhere closely to medically relevant characteristics. These prototypes act as high-level representations of the target image features and are supplied as inputs to the diffusion model. We learn the prototypes of the classes with a different classifier first, and then we start the training of the diffusion model after we initialize the class embeddings with the learned prototypes which are used to guide the diffusion process.

Our model achieves better performance than the original diffusion model when the quality of generated images is compared in terms of clinical validity and biological accuracy.

4.1. Prototype Generation

Each Dataset contains N classes- from each class an equal number of images n are selected for training.

The first step involves extracting the image embeddings using a pretrained CLIP model. The dimension of an embedding is 768. These image embeddings are utilized in the training process as shown in Figure 1 where the prototype representations of each class are learned. The learned prototypes have the same dimension as the input image embeddings. These prototypes differ from the image embeddings themselves in the sense that they provide a representation of the entire class demonstrating intra-class compactness as well as enhancing the differences in feature representation between different classes- inter-class separability. We claim that the prototypes capture the biological intricacies of the different structures in a much better, and using these prototypes for guiding the diffusion process would result in better results than classifier-free guidance using only class labels.

4.2. Diffusion Model Architecture

Our diffusion model architecture follows closely the method proposed by [3], where we initialize the class em-

beddings with the learned prototypes as shown in Figure 2. The difference is that we freeze the weights of the class embeddings and they don't change during the training process. We are concatenating the sinusoidal time embedding t with the prototype m_x that represents the class label of the input x , and obtain \tilde{z} . The core architecture comprises of a UNet-like neural network which is optimized to predict the noise ϵ of the noisy image \tilde{x} added at each timestep t . Over a gradual denoising process, the network is able to produce an image from the learned probability distribution. In order to guide the diffusion process, the class embedding and the time step are also given to the specific layers of the neural network. For the same model training parameters and hyperparameters, the baseline model has randomly initialized class embeddings which are optimized by the diffusion process during training without any explicit optimizations to improve their class representativeness. On the other hand, the prototype-guided model starts with optimized embeddings resulting in better results in a single shot.

5. Experiments

We conduct our experiments on the Bone marrow cell classification dataset and HAM10000 ("Human Against Machine with 10000 training images") dataset - a large collection of multi-source dermatoscopic images of pigmented lesions using 2 NVIDIA A100 GPUs.

5.1. Bone Marrow dataset

The Bone Marrow dataset [17] comprises over 170,000 de-identified, expert-annotated cells derived from the bone marrow smears of 945 patients. These smears were stained using the May-Grünwald-Giemsa/Pappenheim stain. For our experiments, we utilize images categorized into 16 distinct classes, as detailed in Table 1.

5.2. Skin Cancer MNIST: HAM10000

The HAM10000 ("Human Against Machine with 10000 training images") [31] dataset comprises a diverse collection of dermatoscopic images from various populations, acquired using different modalities. The images are categorized into several classes: actinic keratoses and intraepithelial carcinoma/Bowen's disease (akiec), basal cell carcinoma (bcc), benign keratosis-like lesions (solar lentiginos, seborrheic keratoses, and lichen-planus like keratoses, bkl), dermatofibroma (df), melanoma (mel), melanocytic nevi (nv), and vascular lesions (angiomas, angiokeratomas, pyogenic granulomas, and hemorrhage, vasc).

5.3. Image Generation and Feedback

We used a prototype-guided diffusion model trained on real images (64x64 pixels) to generate synthetic image patches. For both datasets, Model training was conducted

Table 1. Classes in the Bone Marrow dataset

Abbreviation	Class Name
ART	Artefact
BAS	Basophil
BLA	Blast
EBO	Erythroblast
EOS	Eosinophil
HAC	Hairy cell
LYT	Lymphocyte
MMZ	Metamyelocyte
MON	Monocyte
MYB	Myelocyte
NGB	Band neutrophil
NGS	Segmented neutrophil
NIF	Not identifiable
PEB	Proerythroblast
PLM	Plasma cell
PMO	Promyelocyte

using 100 images per class. The prototypes are learned using the same images and then these learned prototypes are concatenated with the time embedding and fed as input to different layers of the UNET model.

For the baseline model, similar image size (64x64 pixels) were used to generate the synthetic image patches with 100 images per class. The class embeddings for the baseline are randomly initialized.

In both cases the models are initialized with same set of hyperparameters, values of some of the hyperparameters are mentioned in table 2.

The initial channel size of the UNET model is set to 64 and 4 blocks are utilized for the down and upsampling layers of the model. Each of them has 2 ResNet layers. These layers have a 0.1 Dropout layer. The number of channels keeps on increasing during the Encoder part of the model which is represented by the downsampling layers by a factor of 2,4 and 8. The Decoder part which contains the upsampling layers, mirrors the Encoder, and the channel size keeps on decreasing by the same factors. The final output of the UNET has the same number of channels as the input- 3. This type of hierarchical representation captures both high-level as well as fine features.

For training the diffusion model we employ AdamW optimizer with a learning rate of 0.0001. We resize the images to 64 for both datasets and a per GPU batch size of 16 is employed.

The sampling process involves the generation of 100 images from each class which utilizes faster DDIM sampling [29] over 50 iterations. The generated images are shown in Figures 3 and 6.

For feedback we relied on two domain experts; a pathologist for Bone Marrow dataset and a dermatologist for

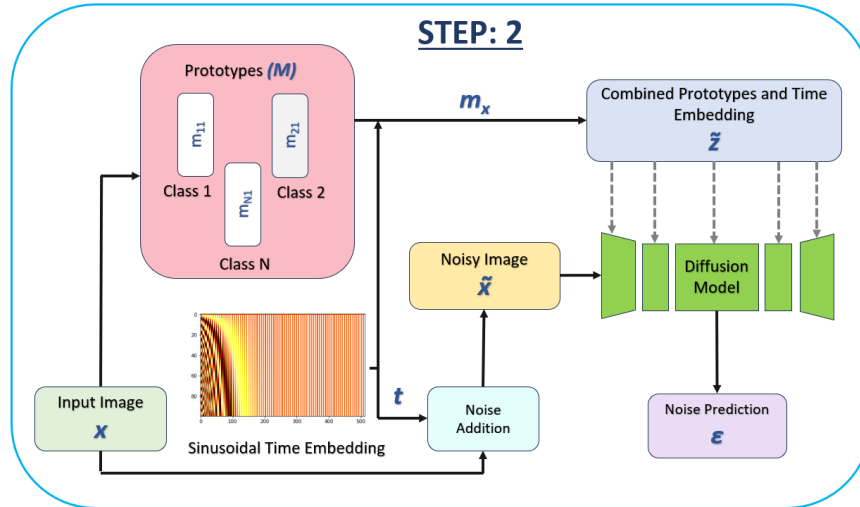


Figure 2. Time embeddings and learnt prototypes are concatenated and passed at various stages in the UNET model to guide the diffusion process

Table 2. Hyperparameters of Diffusion model

Name	Value
Input image size	64
Initial channel size	64
Channel multiplier	[1, 2, 4, 8]
Timesteps	1000
Initial learning rate	1e-4
Number of epochs	1500

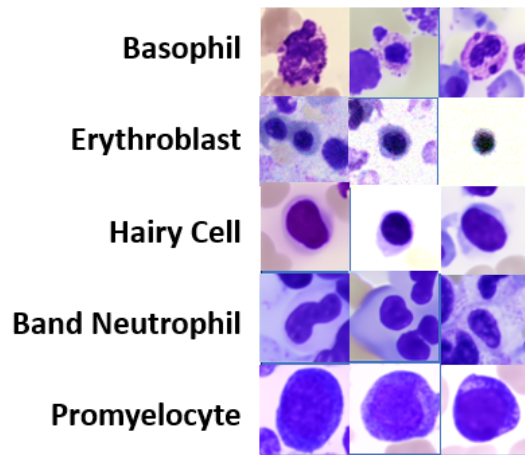


Figure 3. Generated images for 5 classes of Bone Marrow Dataset using Classifier Free Guidance

HAM10000 dataset. Labelstudio was used as a platform for gathering annotations. For Bone Marrow dataset, human expert was provided with plausibility criteria over which contribute to the biological viability of images. These cri-

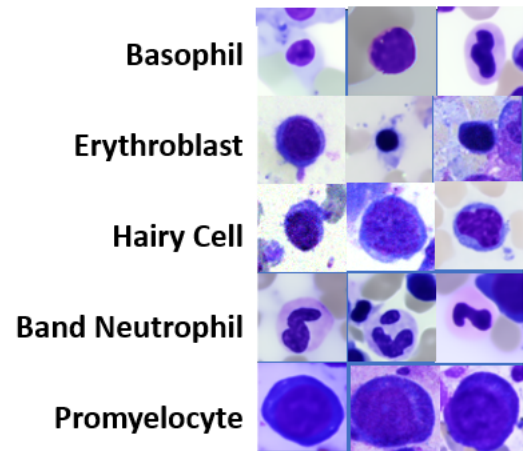


Figure 4. Generated images for 5 classes of Bone Marrow Dataset using Prototype Guidance

teria included cell size, nucleus shape & size, nucleus-to-cytoplasm ratio, cytoplasm color and consistency, chromatin pattern, inclusions, and granules (where appropriate). Failure over any one or more criteria led to the categorization of the image as implausible. Similarly, for HAM10000, the dermatologist was provided with five criteria, all of which are needed to be satisfied for an image to be considered plausible.

6. Results

To evaluate the impact of our proposed architecture on the generation of medically plausible synthetic images, we created two synthetic datasets each for both Bone Marrow

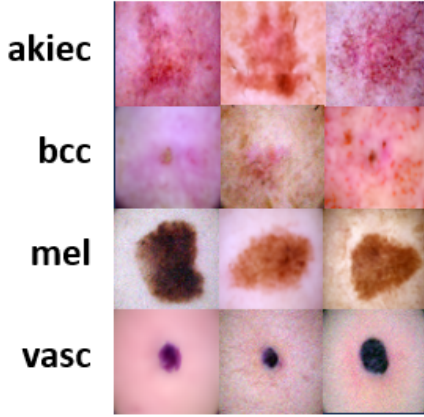


Figure 5. Generated images for 4 classes of Skin Cancer Dataset using Classifier Free Guidance

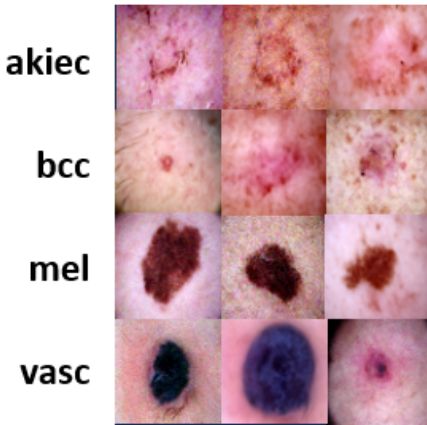


Figure 6. Generated images for 4 classes of Skin Cancer Dataset using Prototype Guidance

dataset and HAM10000 dataset, a sample from the classifier free guidance diffusion model(our baseline) and a sample from prototype guided diffusion model(our approach). For Bone Marrow, each of the two synthetic datasets had 1400 synthetic images(100 images per class). For HAM10000 the sampled quantity was 700 per dataset(here too, 100 images per class). Table 3 lists the fraction of clinically plausible images per cell type for the two synthetic datasets for HAM10000 images as evaluated by an expert dermatologist. As we can see our model provides a significant bump in medical plausibility across all but one cell type. The average rate of clinical plausibility increased from 48.8 % to 60 %.

Table 4 lists the fraction of clinically plausible images per cell type for the two synthetic datasets for Bone Marrow images. For all except two classes we see a substantial increase in the medical plausibility of medical images

Table 3. Comparison of plausibility percentage of synthetic images for HAM10000 dataset

Morphological Cell Type	Baseline (%)	Our Approach (%)
Melanocytic Nevi	68	79
Melanoma	48	65
Benign K-like lesions	46	57
Basal Cell Carcinoma	33	60
Actinic Keratosis	44	49
Vascular Lesions	54	47
Dermatofibroma	49	63

generated. Furthermore, certain cell types such as hairy cells, basophils, and plasma cells are extremely tricky given the nuanced features of each cell type. With these cells, the baseline model substantially struggles to produce medically plausible images; however, we observe a significant improvement through our approach. The average rate of clinical plausibility increased from 48.07 % to 62.57 %.

Table 4. Comparison of plausibility percentage of synthetic images for Bone-Marrow dataset

Morphological Cell Type	Baseline (%)	Our Approach (%)
Plasma Cell	34	56
Erythroblast	66	68
Promyelocyte	48	62
Hairy Cell	21	57
Metamyelocyte	39	53
Band Neutrophil	52	69
Proerythroblast	67	64
Myelocyte	57	56
Monocyte	44	64
Lymphocyte	58	63
Eosinophil	42	71
Segmented Neutrophil	74	78
Blast Cell	45	59
Basophil	26	56

Accuracy in downstream tasks is one of the ways in evaluating the efficacy of synthetic image generation. We evaluated the utility of our model in training a cell-type classification model. In this experiment, we train a ResNext-50 model in classifying 14 cell types for Bone Marrow dataset and seven cell types for HAM1000 dataset once using the classifier free guidance dataset (baseline approach) and then again using our approach. To ensure a fair comparison, the size of synthetic datasets was kept the same. Thereafter, the classification accuracy of both models was tested on a held-out real dataset, containing 50 images per cell type. Classifier trained on real images are used as the baseline. Results are shown in table 5 and table 6 for Bone Marrow and HAM10000 images respectively. As expected, the performance of classification over real images is the best across all metrics showing a significant gap compared to the classifier trained on synthetic images generated using classifier free guidance(baseline). However, our approach helped re-

duce this gap across both datasets to a point where the classifier trained on real images only marginally outperformed the ones trained on our synthetic images.

Table 5. Performance of a classifier trained over real and synthetic images of Bone Marrow dataset

Method	Precision (%)	Recall (%)	F1 Score (%)
Baseline (Classifier Free Guidance)	61.50	65.43	63.40
Ours	72.65	76.64	74.58
Real Images	80.11	79.23	79.66

Table 6. Performance of a classifier trained over real and synthetic images of HAM10000 dataset

Method	Precision (%)	Recall (%)	F1 Score (%)
Baseline (Classifier Free Guidance)	68.95	73.43	71.10
Ours	75.60	74.54	75.08
Real Images	84.56	87.32	85.91

7. Conclusion

Our prototype-guided diffusion framework represents a significant advancement in the field of synthetic medical image generation. By effectively eliminating the need for extensive human feedback, our approach not only reduces the associated costs and time but also produces synthetic images with high medical and biological accuracy. This work paves the way for more efficient and scalable solutions in medical data augmentation, ultimately contributing to the advancement of machine learning in healthcare. Further, Our findings underscore the importance of integrating domain-specific knowledge into generative models and highlight the potential of prototype learning in enhancing the plausibility of synthetic medical images. We believe that our approach will inspire further innovations in the generation of high-quality synthetic medical data, thereby supporting the development of more robust and reliable AI-driven healthcare solutions.

References

- [1] Lisa C Adams, Felix Busch, Daniel Truhn, Marcus R Makowski, Hugo JWL Aerts, and Keno K Bresslem. What does dall-e 2 know about radiology? *Journal of Medical Internet Research*, 25:e43110, 2023. [1](#)
- [2] Hazrat Ali, Shafaq Murad, and Zubair Shah. Spot the fake lungs: Generating synthetic medical images using neural diffusion models. In *Irish Conference on Artificial Intelligence and Cognitive Science*, pages 32–39. Springer, 2022. [1](#), [2](#)
- [3] Gulcin Baykal, Halil Faruk Karagoz, Taha Binhuraib, and Gozde Unal. Protodiffusion: classifier-free diffusion guidance with prototype learning. In *Asian Conference on Machine Learning*, pages 106–120. PMLR, 2024. [3](#), [4](#)
- [4] Andreas Blattmann, Robin Rombach, Kaan Oktay, Jonas Müller, and Björn Ommer. Retrieval-augmented diffusion models. *Advances in Neural Information Processing Systems*, 35:15309–15324, 2022. [2](#)
- [5] Samuel Budd, Emma C Robinson, and Bernhard Kainz. A survey on active learning and human-in-the-loop deep learning for medical image analysis. *Medical image analysis*, 71:102062, 2021. [1](#)
- [6] Pierre Chambon, Christian Bluethgen, Curtis P Langlotz, and Akshay Chaudhari. Adapting pretrained vision-language foundational models to medical imaging domains. *arXiv preprint arXiv:2210.04133*, 2022. [1](#)
- [7] Richard J Chen, Ming Y Lu, Tiffany Y Chen, Drew FK Williamson, and Faisal Mahmood. Synthetic data in machine learning for medicine and healthcare. *Nature Biomedical Engineering*, 5(6):493–497, 2021. [1](#)
- [8] Prafulla Dhariwal and Alexander Nichol. Diffusion models beat gans on image synthesis. *Advances in neural information processing systems*, 34:8780–8794, 2021. [2](#), [3](#)
- [9] Yingjun Du, Zehao Xiao, Shengcai Liao, and Cees Snoek. Protodiff: learning to learn prototypical networks by task-guided diffusion. *Advances in Neural Information Processing Systems*, 36:46304–46322, 2023. [2](#)
- [10] Patrick Esser, Robin Rombach, and Bjorn Ommer. Taming transformers for high-resolution image synthesis. In *Proceedings of the IEEE/CVF conference on computer vision and pattern recognition*, pages 12873–12883, 2021. [2](#)
- [11] Samantha Guerriero, Barbara Caputo, and Thomas Mensink. Deepncm: Deep nearest class mean classifiers. 2018. [2](#)
- [12] Martin Heusel, Hubert Ramsauer, Thomas Unterthiner, Bernhard Nessler, and Sepp Hochreiter. Gans trained by a two time-scale update rule converge to a local nash equilibrium. *Advances in neural information processing systems*, 30, 2017. [2](#)
- [13] Jonathan Ho, Ajay Jain, and Pieter Abbeel. Denoising diffusion probabilistic models. *Advances in neural information processing systems*, 33:6840–6851, 2020. [3](#)
- [14] Jonathan Ho, Chitwan Saharia, William Chan, David J Fleet, Mohammad Norouzi, and Tim Salimans. Cascaded diffusion models for high fidelity image generation. *Journal of Machine Learning Research*, 23(47):1–33, 2022. [2](#)
- [15] Jonathan Ho and Tim Salimans. Classifier-free diffusion guidance. *arXiv preprint arXiv:2207.12598*, 2022. [3](#)
- [16] Junsik Kim, Tae-Hyun Oh, Seokju Lee, Fei Pan, and In So Kweon. Variational prototyping-encoder: One-shot learning with prototypical images. In *Proceedings of the IEEE/CVF conference on computer vision and pattern recognition*, pages 9462–9470, 2019. [2](#)
- [17] Christian Matek, Stephan Krappe, Christian Münzenmayer, Torsten Haferlach, and Carsten Marr. An expert-annotated dataset of bone marrow cytology in hematologic malignancies, 2021. [5](#)
- [18] Gustav Müller-Franzes, Jan Moritz Niehues, Firas Khader, Soroosh Tayebi Arasteh, Christoph Haarburger, Christiane Kuhl, Tianci Wang, Tianyu Han, Teresa Nolte, Sven Nebelung, et al. A multimodal comparison of latent denoising diffusion probabilistic models and generative adversarial networks for medical image synthesis. *Scientific Reports*, 13(1):12098, 2023. [2](#)

- [19] Kai Packhäuser, Lukas Folle, Florian Thamm, and Andreas Maier. Generation of anonymous chest radiographs using latent diffusion models for training thoracic abnormality classification systems. In *2023 IEEE 20th International Symposium on Biomedical Imaging (ISBI)*, pages 1–5. IEEE, 2023. [1](#)
- [20] Walter HL Pinaya, Petru-Daniel Tudosiu, Jessica Dafflon, Pedro F Da Costa, Virginia Fernandez, Parashkev Nachev, Sebastien Ourselin, and M Jorge Cardoso. Brain imaging generation with latent diffusion models. In *MICCAI Workshop on Deep Generative Models*, pages 117–126. Springer, 2022. [2](#)
- [21] Alec Radford, Jong Wook Kim, Chris Hallacy, Aditya Ramesh, Gabriel Goh, Sandhini Agarwal, Girish Sastry, Amanda Askell, Pamela Mishkin, Jack Clark, et al. Learning transferable visual models from natural language supervision. In *International conference on machine learning*, pages 8748–8763. PMLR, 2021. [2](#)
- [22] Muhammad Imran Razzak, Saeeda Naz, and Ahmad Zaib. Deep learning for medical image processing: Overview, challenges and the future. *Classification in BioApps: Automation of decision making*, pages 323–350, 2018. [1](#)
- [23] Mehdi SM Sajjadi, Olivier Bachem, Mario Lucic, Olivier Bousquet, and Sylvain Gelly. Assessing generative models via precision and recall. *Advances in neural information processing systems*, 31, 2018. [2](#)
- [24] Tim Salimans and Jonathan Ho. Progressive distillation for fast sampling of diffusion models. *arXiv preprint arXiv:2202.00512*, 2022. [2](#)
- [25] Christoph Schuhmann, Romain Beaumont, Richard Vencu, Cade Gordon, Ross Wightman, Mehdi Cherti, Theo Coombes, Aarush Katta, Clayton Mullis, Mitchell Wortsman, et al. Laion-5b: An open large-scale dataset for training next generation image-text models. *Advances in Neural Information Processing Systems*, 35:25278–25294, 2022. [1](#)
- [26] Yu Shu, Yemin Shi, Yaowei Wang, Tiejun Huang, and Yonghong Tian. P-odn: Prototype-based open deep network for open set recognition. *Scientific reports*, 10(1):7146, 2020. [2](#)
- [27] Jake Snell, Kevin Swersky, and Richard Zemel. Prototypical networks for few-shot learning. *Advances in neural information processing systems*, 30, 2017. [2](#)
- [28] Jascha Sohl-Dickstein, Eric Weiss, Niru Maheswaranathan, and Surya Ganguli. Deep unsupervised learning using nonequilibrium thermodynamics. In *International conference on machine learning*, pages 2256–2265. PMLR, 2015. [2](#)
- [29] Jiaming Song, Chenlin Meng, and Stefano Ermon. Denoising diffusion implicit models. *arXiv preprint arXiv:2010.02502*, 2020. [2](#), [5](#)
- [30] Shenghuan Sun, Greg Goldgof, Atul Butte, and Ahmed M Alaa. Aligning synthetic medical images with clinical knowledge using human feedback. *Advances in Neural Information Processing Systems*, 36, 2024. [1](#), [2](#)
- [31] Philipp Tschandl. The HAM10000 dataset, a large collection of multi-source dermatoscopic images of common pigmented skin lesions, 2018. [5](#)
- [32] Stefan Winkler and Praveen Mohandas. The evolution of video quality measurement: From psnr to hybrid metrics. *IEEE transactions on Broadcasting*, 54(3):660–668, 2008. [2](#)
- [33] Zheng Wu, Kehua Guo, Entao Luo, Tian Wang, Shoujin Wang, Yi Yang, Xiangyuan Zhu, and Rui Ding. Medical long-tailed learning for imbalanced data: bibliometric analysis. *Computer Methods and Programs in Biomedicine*, page 108106, 2024. [1](#)
- [34] Zhirong Wu, Yuanjun Xiong, Stella X Yu, and Dahua Lin. Unsupervised feature learning via non-parametric instance discrimination. In *Proceedings of the IEEE conference on computer vision and pattern recognition*, pages 3733–3742, 2018. [2](#)
- [35] Hong-Ming Yang, Xu-Yao Zhang, Fei Yin, and Cheng-Lin Liu. Robust classification with convolutional prototype learning. In *Proceedings of the IEEE conference on computer vision and pattern recognition*, pages 3474–3482, 2018. [3](#)
- [36] Tianfei Zhou, Wenguan Wang, Ender Konukoglu, and Luc Van Gool. Rethinking semantic segmentation: A prototype view. In *Proceedings of the IEEE/CVF Conference on Computer Vision and Pattern Recognition*, pages 2582–2593, 2022. [2](#)